Scripta Materialia 153 (2018) 118–121

Contents lists available at ScienceDirect

Scripta Materialia

journal homepage: www.elsevier.com/locate/scriptamat

Regular article

An in situ neutron diffraction study of plastic deformation in a $Cu_{46.5}Zr_{46.5}Al_7$ bulk metallic glass composite☆

D.M. Wang [a,b,c], Y. Chen [b], J. Mu [a], Z.W. Zhu [d], H.F. Zhang [d], Y.D. Wang [a,*], K. An [b,*]

[a] Key Laboratory for Anisotropy and Texture of Materials (Ministry of Education), School of Material Science and Engineering, Northeastern University, Shenyang 110819, PR China
[b] Neutron Scattering Division, Oak Ridge National Laboratory, Oak Ridge, TN 37831, USA
[c] Shull Wollan Center, Oak Ridge National Laboratory, Oak Ridge, TN 37831, USA
[d] Shenyang National Laboratory for Materials Science, Institute of Metal Research, Chinese Academy of Sciences, Shenyang 110016, PR China

ARTICLE INFO

Article history:
Received 11 March 2018
Received in revised form 6 May 2018
Accepted 8 May 2018
Available online xxxx

Keywords:
Bulk metallic glass composite
In situ neutron diffraction
Micro-mechanical behaviors
Amorphous
Load transfer

ABSTRACT

Micro-mechanical behaviors of a $Cu_{46.5}Zr_{46.5}Al_7$ bulk metallic glass composite in the plastic regime were investigated by continuous in situ neutron diffraction during compression. Three stages of the plastic deformation were observed according to the work-hardening rate. The underlying natures of the work hardening, correlating with the lattice/microscopic strain evolution, are revealed for the three stages: (1) the initiation of shear bands, (2) the phase load transferring from the amorphous phase to the B2 phase and (3) the accelerated martensitic transformation and the work hardening of the polycrystalline phases promoted by the rapid propagation of the shear bands.

The resistance to catastrophic fracture of bulk metallic glasses (BMGs) due to localized shear deformation [1,2] has been improved by introducing in situ crystalline precipitates into the amorphous matrix [3,4], i.e., in situ bulk metallic glass composites (BMGCs). The crystalline reinforcement in the in situ BMGCs is believed to promote the multiplication of the shear bands and inhibit their rapid propagation, thereby leading to improved plasticity [5,6]. In particular, large tensile plasticity [4,7,8] up to 15.5% [7] was achieved in a series of ZrTi-based BMGCs owing to the inhibition of local deformation in the glassy matrix. However, most of the in situ BMGCs show work softening after yielding instead of work hardening, which restricts their engineering applications. This behavior is observed because the accumulations of dislocations in the crystalline and amorphous phase interfaces fail to provide a sufficient counterbalance to the softening of amorphous matrix [4,7–10] when the crystallites in the composites deform via dislocation movements. CuZr-based shape memory bulk metallic glass composites (SM-BMGCs), which have recently been developed, possess high strength, enhanced ductility and work-hardening ability [2,11,12], which probably originated from the intrinsic pronounced work hardening and superelasticity of the B2-CuZr phase [13]. These new CuZr-based SM-BMGCs have gained considerable interest in the past toward understanding the deformation mechanism [2,14–17]. For examples, the high compatibility of elastic properties of the B2 and amorphous phases was thought to be essential for the ductility [14]; the intrinsic work hardening of B2 phase could avoid necking in the BMGC [17] etc. However, most of the reported studies were based on the traditional ex situ approaches, which are indirect and ambiguous for studying a deformation mechanism involving a reversible phase transformation [18].

To monitor material deformation and phase transformation with a reversible behavior, in situ techniques are superior to the traditional ex situ approaches [18–20]. Recently, in situ diffraction was used to reveal the micro-mechanical behaviors of BMGCs in the elastic or quasi-elastic stage [21–26]. For example, the deviation of the Cu-Zr-Al-Co SM-BMGC from the macro-linear stage [21,22], i.e., macroscopic yielding, was just followed by the martensitic transformation (MT) [21,22], and the same threshold lattice strain was required to initiate the MT for the samples with different volume fractions of the B2 phase [21]. The micro-mechanical behaviors differ with Co concentration [21,22], which signifies that the composition plays a key role in the mechanical properties of CuZr-based SM-BMGCs. However, due to the lack of in situ data of amorphous phase deformation, the understanding of the micro-mechanical behaviors of CuZr-based SM-BMGCs in the

☆ This manuscript has been authored by UT-Battelle, LLC under Contract No. DE-AC05-00OR22725 with the U.S. Department of Energy. The United States Government retains and the publisher, by accepting the article for publication, acknowledges that the United States Government retains a non-exclusive, paid-up, irrevocable, world-wide license to publish or reproduce the published form of this manuscript, or allow others to do so, for United States Government purposes. The Department of Energy will provide public access to these results of federally sponsored research in accordance with the DOE Public Access Plan (http://energy.gov/downloads/doe-public-access-plan).

* Corresponding authors.
E-mail addresses: ydwang@mail.neu.edu.cn (Y.D. Wang), kean@ornl.gov (K. An).

https://doi.org/10.1016/j.scriptamat.2018.05.012
1359-6462/

plastic deformation regime with work hardening remains unclear: how does the load transfer between the B2 and amorphous phases as well as the newly formed phase in the plastic regime, and what is the effect of stress redistributions on the work-hardening characteristics in the CuZr-based SM-BMGCs? In this paper, the $Cu_{46.5}Zr_{46.5}Al_7$ SM-BMGC under uniaxial compression was investigated by in situ neutron diffraction (ND). Through the visualization of the MT and the lattice/microscopic strain evolution of both the crystalline and amorphous phases, the micro-mechanical behaviors in the plastic regime were elucidated, as were their correlation to the work-hardening rate variation.

$Cu_{46.5}Zr_{46.5}Al_7$ (nominal at.%) ingots were synthesized by arc melting of the pure constituent elements under a Ti-getter high-purity argon atmosphere followed by injection into a copper mold to obtain cylindrical specimens with a diameter of 4 mm and a length of 8 mm for the compression experiments. The microstructure of the as-cast sample was characterized by a QUANTA 600 scanning electron microscope (SEM).

In situ ND experiment was performed at the VULCAN engineering materials diffractometer, Spallation Neutron Source (SNS), Oak Ridge National Laboratory (ORNL) [27]. The specimen was mounted horizontally in the VULCAN loadframe with the axial direction parallel to the loading direction (LD), as shown in Supplement A (Fig. A.1). Details about the in situ ND experiment setup can be found elsewhere [18–20,27]. The specimen was evaluated with two loading-unloading uniaxial compression cycles. Different peak stresses for each cycle −990 MPa and −1825 MPa were applied respectively for capturing the deformation characteristics with the different stress maxima. Before compression, the sample was pre-compressed up to −215 MPa and then unloaded to −5 MPa to remove sluggish gaps between the sample and the platens. Considering the weak scattering ability of the amorphous phase, the strain rate was designed to be as low as $2.5 \times 10^{-6}\ s^{-1}$ to ensure sufficient ND statistics.

The in situ ND data were continuously recorded throughout the deformation and then were sliced with a 5-minute interval by VDRIVE software [28]. Fig. A.2(a) shows an example of the ND pattern along the LD before loading. It shows sharp peaks of the B2 phase with a primitive cubic structure as well as small peaks of minor $AlCu_2Zr$ phase superimposing on the broad scattering amorphous hump, as determined by full-pattern Rietveld refinement via Generalized Structure Analysis Software (GSAS) [29]. As shown in the SEM micrograph in Fig. A.2(b), the dark spherical B2 grains with uneven sizes distribute in the bright amorphous matrix, and most of the B2 grains mutually impinged on each other. The initial volume fraction of the B2 phase is determined to be approximately 40% by calculating the contrast from the SEM micrograph using ImageTool software.

To align with the focus of this paper on the BMGC plasticity, the 2nd cycle with profound plastic deformation is mainly discussed here while the results of the 1st cycle showing little plasticity are presented in Supplement A. Fig. 1(a) depicts the stress-strain (S—S) curve of the BMGC in the 2nd cycle under compression. The sample started to yield, as indicated by the change of curve linearity, below the apparent yield point of −1490 MPa, followed by hardening and plastic deformation to a total strain of −6% at the peak stress of −1825 MPa. After unloading, there is −3.6% residual strain. Based on the change in the work-hardening rate in Fig. 1(b), the plastic regime of the studied BMGC is divided into three stages. First, in Stage I ($\sigma < -1651$ MPa), the work-hardening rate drops drastically right after the yielding; then in Stage II ($-1651\ MPa < \sigma < -1724\ MPa$), the transition stage, the reduction in the work-hardening rate slows down; and last, in Stage III ($\sigma > -1724$ MPa), the work-hardening rate shows a relatively small slope.

In situ ND shows the phase transformation evolution upon loading, as depicted by evolution in the ND patterns in the LD under various applied stresses in the 2nd cycle in Fig. 2. With increasing compressive stress, a new peak at the d-space of 2.06 Å appeared at a stress of −989 MPa, which was identified as the $(020)_{B19'}$ reflection of B19′ martensite with a monoclinic structure as determined by the Rietveld refinement (Fig. A.3). Continued loading resulted in increase in the intensities of the B19′ martensite peaks and corresponding decrease in the intensities of the B2 phase peaks, indicating the progression of the phase transformation. However, the reversion of those peaks' intensities was not that responsive upon stress removal, and only slight intensity changes were observed after complete unloading. Therefore, the transformation back to the B2 phase was highly limited in this CuZr-based SM-BMGC.

Quantitatively, full-pattern Rietveld refinements were conducted on the chopped diffraction data to obtain phase volume fractions by using a cylindrical symmetry texture model in GSAS [29]. The B2 and B19′ volume fractions as functions of the applied stress and strain in the 2nd cycle are shown in Fig. 3(a) and (b), respectively. The accumulated B19′ phase is refinable after approximately −1200 MPa loading, at which formation of the new phase reaches the minimum limit of Rietveld refinement. Under −1825 MPa (−6% strain), the studied BMGC contains about 22 vol% martensite phase, which is small compared to the amount of MT that occurred in the pure B2 phase under −1220 MPa (−6.8% strain) [18]. It is likely that the confinement of B2 in the amorphous matrix constrains the MT due to load sharing taken by the amorphous phase. In contrast to a nonlinear dependence of stress, the volume fractions versus the strain exhibits a linear relationship during the deformation, as shown in Fig. 3(b), which confirms that the MT is induced mainly by strain instead of stress [18,21]. The change of the volume fraction in Fig. 3(a) matched the three plastic deformation stages defined above. In Stage I, the phase transformation rate was slow as indicated by the low slope. Then, the transformation accelerated with stress value higher than −1651 MPa, as observed in Stage II. In Stage III, when the stress increased to −1724 MPa, the

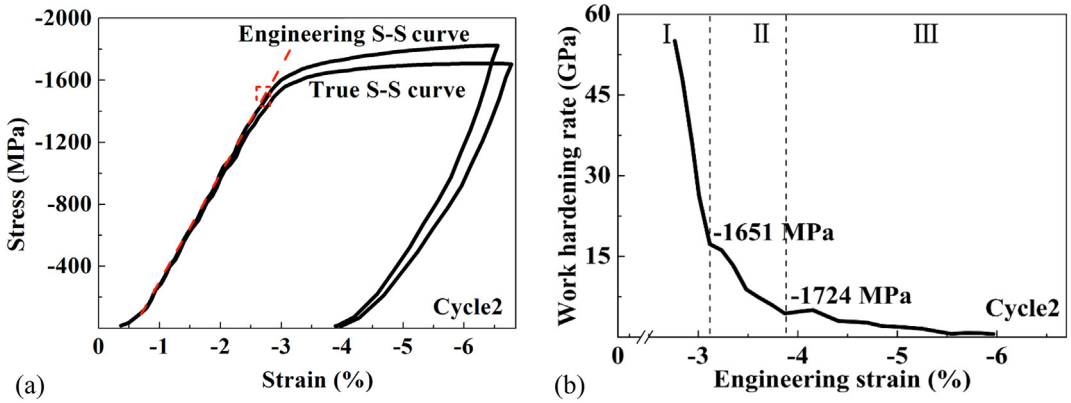

Fig. 1. Measured compressive stress-strain curve of the $Cu_{46.5}Zr_{46.5}Al_7$ BMGC in the 2nd cycle; (b) work-hardening rate vs. strain in the 2nd cycle.

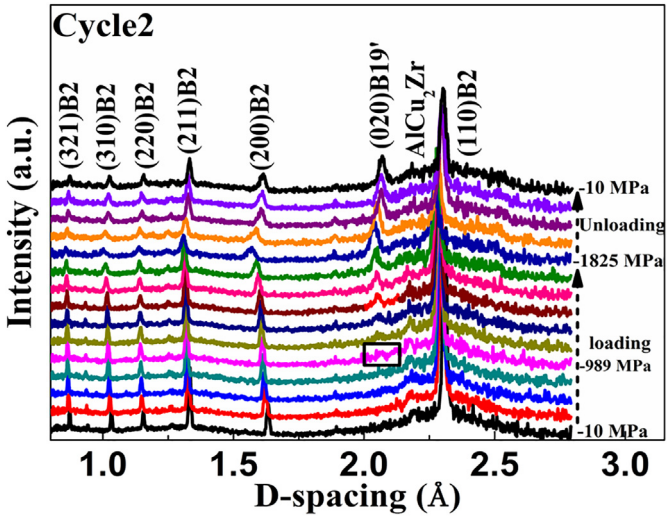

Fig. 2. Neutron diffraction patterns at various stress levels with respect to the loading direction in the 2nd cycle for the studied $Cu_{46.5}Zr_{46.5}Al_7$ BMGC.

phase transformation rate further increased in comparison with that in stage II, as demonstrated by the gradually vertical increase in the B19′ phase volume fraction.

The MT clearly determines the micro-mechanical deformation behaviors [21–23], and the behaviors are further studied through the evolution of lattice/microscopic strains (ε) or microstresses (σ) obtained from the in situ ND experiments, as often shown in many composite materials [18,19,23]. For the amorphous phase, the diffuse diffraction patterns were first extracted from the ND patterns, followed by calculating the relative position change in the first sharp diffraction peak (FSDP) by referring to the initial load to obtain the microscopic strain [21,30-32]. For the B2 and B19′ phases, single peak fitting was conducted on the ND patterns to obtain their lattice strains of certain grain groups [18,21]. The microstress of the different grain groups with their plane normal $\langle hkl \rangle$ parallel to the LD, such as the $(110)_{B2}$, $(211)_{B2}$, $(310)_{B2}$ and $(020)_{B19'}$ reflections and the FSDP, can be obtained by Hooke's law: $\sigma = E{\cdot}\varepsilon$, where E is the diffraction elastic constants chosen from references ([18] for the B2, B19′ and [14] for the amorphous phase, respectively).

Fig. 4(a) shows the measured lattice/microscopic strains vs. the stress and the calculated microstresses vs. the strain are shown in Fig. 4(b). For clarity, the lattice strain changes of the B2 phase in the plastic regime in Fig. 4(a) is enlarged and shown in Fig. A.7. In the initial stage of deformation, all the reflections of the B2 phase and the FSDP of the amorphous phase showed a linear relationship with the applied stress. After −660 MPa, the $(110)_{B2}$ reflection started to respond nonlinearly and the FSDP concurrently showed an opposite deviation trend. This deviation implies the occurrence of slip in the grains [33] or the onset of the MT [18]. Combined with the discussion on the micro-mechanical deformation behaviors during the 1st cycle in Supplement A, the $(110)_{B2}$ lattice strain vs. applied stress deviated at −696 MPa, while the extremely small residual lattice strain and full width at half maximum (FWHM) in Fig. A.5(a) and (b) were obtained after complete unloading. However, no obvious martensite peak was detected by the in situ ND as shown in Fig. A.4(b), due to the nano-sized martensite formation under lower stress which was beyond the ND ability but observed by TEM [16]. Therefore, this deviation at the stress of −660 MPa in the 2nd cycle is a convolution of the formation of the nano-martensite and the slip in the grains. More load was transferred to the amorphous phase due to the strain relaxation in the B2 grains as evidenced by the increase in the slope of lattice strain vs. applied stress of $(110)_{B2}$ and the corresponding decrease in its amorphous counterpart (FSDP) displayed in Fig. 4(a). This can be easily seen as the increase in the microstress of the amorphous phase in Fig. 4(b). With the increase of applied stress, other lattice planes started gradually deflecting until the first B19′ peak was observed at the stress of −989 MPa. Furthermore, the MT and the plastic deformation of the B2 phase progressed continuously, and the applied load carried by the amorphous phase finally reached its limit at a stress of −1490 MPa in Fig. 4(b). It is also demonstrated in Fig. 4(a) by the almost constant FSDP microscopic strain of the amorphous phase. This observation implies that the shear bands eventually initiated from the amorphous matrix [21], as observed by SEM after fracture in Fig. A.8, and hence, the sample started to undergo obvious plastic deformation.

As such, the three-stage plastic behavior in this CuZr-based SM-BMGC is well characterized by the in situ ND observations, and the underlying mechanisms are revealed. In Stage I, the early stage of the macro plastic deformation, the initiation of the shear bands in the amorphous matrix dominates the plastic deformation. As the amorphous phase becomes softened, the applied load starts to transfer to other grains in the crystalline phase. This results in a reduction of microscopic strain increment in the amorphous phase while an increasing change of the B19′ (020) microstress and, on a macroscopic scale, the rapid decrease of work-hardening rate in Fig. 1(b).

In Stage II, the plastic deformation of the B2 phase mainly correlates with the relatively slow decrease of the work-hardening rate. In this stage, the microscopic strain in the amorphous phase does not continue increasing but starts to decrease. Simultaneously, the lattice strains of the B2 phase are further deflected. More of the applied load was transferred to the crystalline phases as the B2 microstresses increased [Fig. 4(b)]. The plastic deformation results from slips in B2 phase, as evidenced by the decreasing slope of the lattice strains vs. applied stress curves [Fig. 4(a)] and by the rapid growth of the FWHM values [Fig. A.9], which are closely related to the increase in dislocation density when

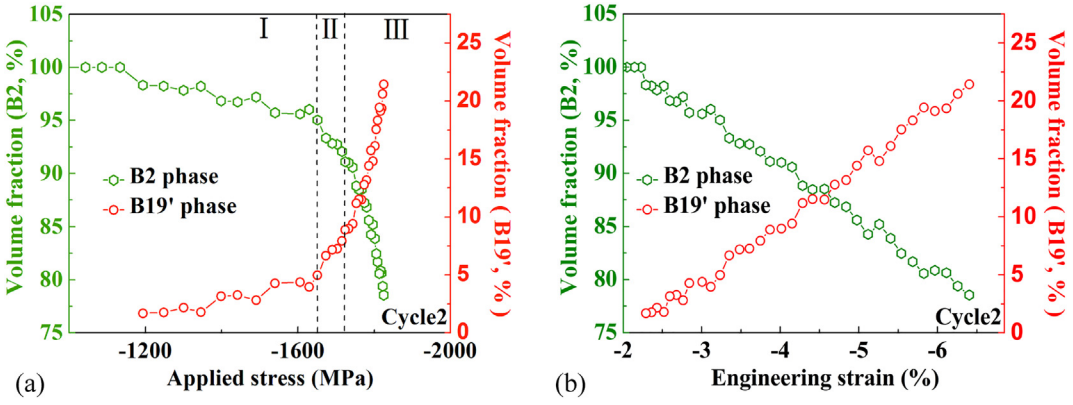

Fig. 3. Responses of the volume fractions of B2 and B19′ phases in the studied $Cu_{46.5}Zr_{46.5}Al_7$ BMGC as a function of (a) applied stress and (b) strain with respect to the loading direction in the 2nd cycle.

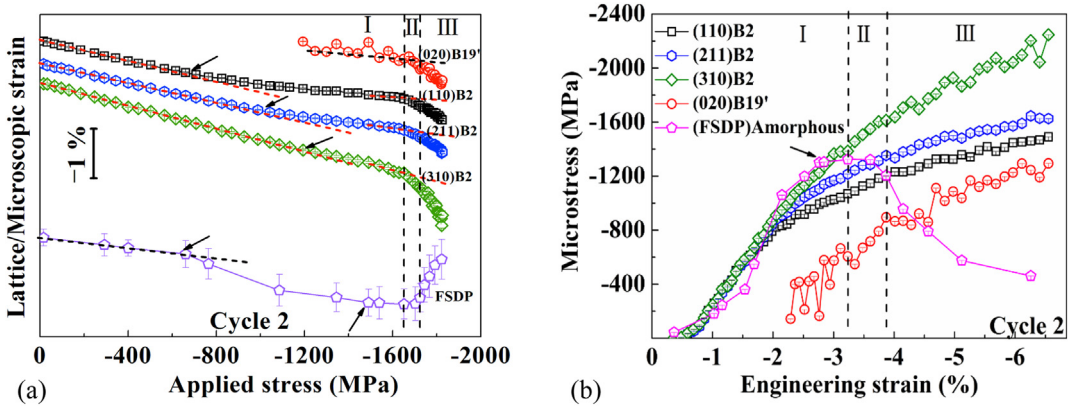

Fig. 4. Evolution of (a) lattice/microscopic strains and (b) microstresses along the loading axis in regard to $(020)_{B19'}$, $(110)_{B2}$, $(211)_{B2}$, $(310)_{B2}$ and the amorphous phase (FSDP) as a function of applied stress or strain during loading in the 2nd cycle for the studied $Cu_{46.5}Zr_{46.5}Al_7$ BMGC.

slip occurs [18,34]. Due to the development of shear bands in Stage I, the confinement effect from the amorphous matrix on the MT is reduced, and thus, the MT rate starts increasing [Fig. 3(a)]. The amount of martensite is too low (9 vol%) to majorly contribute to the deformation until Stage III.

In Stage III, the amorphous phase relaxes, and the accelerated MT plays a key role in the change of work-hardening rate. After Stage II, the microscopic strain in the amorphous phase reduced quickly after a stress of −1724 MPa [Fig. 4(a)]. This result is different from those of previous reports [18,21,33]. The amorphous phase is well known to deform plastically through the propagation of the shear bands. Thus, this phenomenon is undoubtedly associated with the movement of the shear bands, which results in the amorphous phase stress partition relief and further reduction of the confinement on the B2 phase. As a result, the microstress of the amorphous phase drops rapidly [Fig. 4(b)]. While the sample still shows work hardening, the relaxation of the amorphous phase leads to more and quicker load sharing in the B2 phase, therefore inducing an accelerated MT in Stage III. As the volume fraction of B19′ quickly increases, the volume change during the MT considerably contributes to the plasticity, and this newly formed martensite phase takes load sharing together with the remnant B2 phase, as evidenced by the quick uptake of the B19′ lattice strain.

In summary, the plastic deformation stage in the $Cu_{46.5}Zr_{46.5}Al_7$ BMGC was explicitly investigated by in situ ND. The three-stage deformation characteristics of the plastic regime were clearly and comprehensively revealed by lattice/microscopic strains of the constituent phases in the BMGC and the work-hardening rate variations. This research not only has important implications for the understanding of the plastic deformation mechanism for the CuZr-based SM-BMGCs but also is beneficial to other BMGCs with different alloy systems.

Acknowledgements

In situ neutron diffraction experiments were carried out at SNS, ORNL, supported by the U.S. Department of Energy, Basic Energy Sciences, Scientific User Facilities Division. D.M. Wang is grateful for the financial support provided by the China Scholarship Council (CSC) during the visit to ORNL and the University of Tennessee, Knoxville (UTK). Y.D Wang, J. Mu and D.M. Wang acknowledge the financial support from the National Natural Science Foundation of China (NSFC) (Grant Nos. 51771049 and 5179480014), and State Key Lab of Advanced Metals and Materials (No. 2016-Z06). The authors thank Mr. M. Frost, Mr. H. Skorpenske from ORNL, Mr. T.K. Liu from the UTK and Dr. H.M. Fu, Mr. D.M. Liu, Mr. S. Chen, Mr. H.Y. Lu and Mr. S.F. Lin from Shenyang Chinese Academy of Sciences for their technical assistance in this research.

Appendix A. Supplementary data

Supplementary data to this article can be found online at https://doi.org/10.1016/j.scriptamat.2018.05.012.

References

[1] C.A. Pampillo, J. Mater. Sci. 10 (1975) 1194–1227.
[2] S. Pauly, S. Gorantla, G. Wang, U. Kühn, J. Ecker, Nat. Mater. 9 (2010) 473–477.
[3] J. Das, M.B. Tang, K.B. Kim, R. Theissmann, F. Baier, W.H. Wang, J. Eckert, Phys. Rev. Lett. 94 (2005), 205501.
[4] D.C. Hofmann, J.Y. Suh, A. Wiest, G. Duan, M.L. Lind, M.D. Demetriou, W.L. Johnson, Nature 451 (2008) 1085–1089.
[5] J. Eckert, J. Das, S. Pauly, C. Duhamel, J. Mater. Res. 22 (2007) 285–301.
[6] C. Schuh, T. Hufnagel, U. Ramamurty, Acta Mater. 55 (2007) 4067–4109.
[7] J.W. Qiao, A.C. Sun, E.W. Huang, Y. Zhang, P.K. Liaw, C.P. Chuang, Acta Mater. 59 (2011) 4126–4137.
[8] J.W. Qiao, S. Wang, Y. Zhang, P.K. Liaw, G.L. Chen, Appl. Phys. Lett. 94 (2009) 151905.
[9] D.C. Hofmann, J.Y. Suh, A. Wiest, M.L. Lind, M.D. Demetriou, W.L. Johnson, PNAS 105 (2008) 20136.
[10] J. Qiao, H. Jia, P.K. Liaw, Mater. Sci. Eng. R 100 (2016) 1–69.
[11] D.C. Hofmann, Science 329 (2010) 1294–1295.
[12] Y. Wu, Y. Xiao, G. Chen, C.T. Liu, Z. Lu, Adv. Mater. 22 (2010) 2770–2773.
[13] D. Schryvers, G.S. Firstov, J.W. Seo, J. Van Humbeeck, Yu.N. Koval, Scr. Mater. 6 (1997) 1119–1125.
[14] S. Pauly, G. Liu, G. Wang, J. Das, K.B. Kim, U. Kühn, D.H. Kim, J. Eckert, Appl. Phys. Lett. 95 (2009), 101906.
[15] Y. Wu, H. Wang, X.J. Liu, X.H. Chen, X.D. Hui, Y. Zhang, Z.P. Lu, J. Mater. Sci. Technol. 30 (2014) 566–575.
[16] K.K. Song, S. Pauly, Y. Zhang, R. Li, S. Gorantla, N. Narayanan, U. Kühn, T. Gemming, J. Eckert, Acta Mater. 60 (2012) 6000–6012.
[17] S. Pauly, G. Liu, G. Wang, U. Kühn, N. Mattern, J. Eckert, Acta Mater. 57 (2009) 5445–5453.
[18] D.M. Wang, J. Mu, Y. Chen, Y.M. Qi, W. Wu, Y.D. Wang, H.J. Xu, H.F. Zhang, K. An, J. Alloys Compd. 696 (2017) 1096–1104.
[19] D. Yu, K. An, Y. Chen, X. Chen, Scr. Mater. 89 (2014) 45–48.
[20] W. Wu, K. An, L.K. Huang, S.Y. Lee, P.K. Liaw, Scr. Mater. 69 (2013) 358–361.
[21] Y. Wu, D. Ma, Q.K. Li, A.D. Stoica, W.L. Song, H. Wang, X.J. Liu, G.M. Stoica, G.Y. Wang, K. An, X.L. Wang, M. Li, Z.P. Lu, Acta Mater. 124 (2017) 478–488.
[22] G. Song, C. Lee, S.H. Hong, K.B. Kim, S.Y. Chen, D. Ma, K. An, P.K. Liaw, J. Alloys Compd. 723 (2017) 714–721.
[23] J. Mu, Z.W. Zhu, R. Su, Y.D. Wang, H.F. Zhang, Y. Ren, Acta Mater. 61 (2013) 5008–5017.
[24] L.L. Ma, L. Wang, Y.F. Xue, Y.D. Wang, N. Li, Y. Ren, H.F. Zhang, A.M. Wang, Mater. Sci. Eng. A 530 (2011) 344–348.
[25] X.Q. Zhang, L. Wang, Q.B. Fan, Y.F. Xue, Y.D. Wang, Z.H. Nie, H.F. Zhang, H.M. Fu, Mater. Sci. Eng. A 598 (2014) 407–412.
[26] H. Suzuki, J. Saida, H. Kato, A.D. Setyawan, M. Imafuku, Scr. Mater. 60 (2009) 725–728.
[27] K. An, H.D. Skorpenske, A.D. Stoica, D. Ma, X.L. Wang, E. Cakmak, Metall. Mater. Trans. A 42 (2011) 95–99.
[28] K. An, ORNL Report, ORNL-TM-2012-621, Oak Ridge National Laboratory, 2012.
[29] A.C. Larson, R.B. Von Dreele, General Structure Analysis System, LANSCE, MS-H805, Los Alamos, New Mexico, 1994.
[30] T.C. Hufnagel, R.T. Ott, J. Almer, Phys. Rev. B 73 (2006) 064204.
[31] H.F. Poulsen, J.A. Wert, J. Neuefeind, V. Honkimaki, M. Daymond, Nat. Mater. 4 (2005) 33–36.
[32] Y.J. Huang, J.C. Khong, T. Connolley, J. Mi, Appl. Phys. Lett. 104 (2014) 031912.
[33] M.T. Hutchings, P. Withers, T. Holden, T. Lorentzen, Introduction to the Characterization of Residual Stress by Neutron Diffraction, CRC Press, Boca Raton, FL, 2005.
[34] P. Sedmak, P. Sittner, J. Pilch, C. Curfs, Acta Mater. 94 (2015) 257–270.